# Supporting Information

## In/ZnO@C hollow nanocubes for efficient electrochemical reduction of $CO_2$ to formate and rechargeable $Zn$-$CO_2$ batteries

Xue Teng[a], Yanli Niu[a], Shuaiqi Gong[a], Mingze Xu[a], Xuan Liu[a], Lvlv Ji[b] and Zuofeng

Chen*,[a]

[a]School of Chemical Science and Engineering, Tongji University, 1239 Siping Road,

Shanghai 200092, China

[b]School of Materials Science and Engineering, Zhejiang Sci-Tech University,

Hangzhou 310018, China

* zfchen@tongji.edu.cn (Z.-F. C.)

## EXPERIMENTAL

**Chemicals.** Indium nitrate ($In(NO_3)_3$, 99.9%), zinc nitrate hexahydrate ($Zn(NO_3)_2 \cdot 6H_2O$, 98%), 2-methylimidazole (2-MeIM, 98%), potassium bicarbonate ($KHCO_3$, > 99.5%) and hexadecyl trimethyl ammonium bromide (CTAB, 99%) were obtained from MACKLIN. All the chemicals were used without further purification. Deionized water (18.0 MΩ cm) was used in all experiments.

**Apparatuses.** Scanning electron microscopy (SEM) images and energy dispersive X-ray spectroscopy (EDX) data were obtained at Hitachi S-4800 (Hitachi, Japan) equipped with a Horiba EDX system (X-max, silicon drift X-Ray detector). Transmission electron microscopy (TEM) images, high resolution TEM (HRTEM) images and selected area electron diffraction (SAED) image were obtained using Tecnai G2 F20 S-Twin. The high-angle annular dark-field scanning TEM (HAADF-STEM) and EDX mapping images were obtained from FEI Talos 200x. The powder X-ray diffraction (XRD) patterns of the as-prepared catalysts were collected with Bruker Foucs D8 Advanced via ceramic monochromatized Cu Kα radiation of 1.54178 Å, operating at 40 kV and 40 mA. X-ray photoelectron spectra (XPS) were recorded on a Kratos Axis Ultra DLD X-ray Photoelectron Spectrometer using 60 W monochromated Mg Kα radiation as the X-ray source for excitation. Raman spectra were obtained on a confocal microscope laser Raman spectrometer (Rainshaw invia). Fourier Transform Infrared (FT-IR) spectra were obtained on a Nicolet 6700 spectrometer (Thermo Fisher Nicolet IS10, USA) with KBr pellets. The elemental contents of Zn and In were measured on a Perkin Elmer Inductively Coupled Plasma (ICP Optima 8300).

**Procedures.** *Synthesis of In/ZnO@C hollow nanocubes.* 160 mg of Zn(NO$_3$)$_2$·6H$_2$O, 80 mg of In(NO$_3$)$_3$ and 4 mg of CTAB were dissolved in 8 mL purified water to obtain a homogeneous solution. The above solution was rapidly poured into 56 mL of aqueous solution with 3.632 g of 2-MeIM under vigorous stirring at room temperature for 0.5 h. The resultant mixture (denoted as In(OH)$_3$-Zn-MOF) was centrifuged and the obtained white precipitate was washed with water, and then dried in an oven at 60 °C overnight. Finally, the In(OH)$_3$-Zn-MOF was carbonized at 600 °C for 2 h with a heating rate of 5 °C min$^{-1}$ under Ar to obtain In/ZnO@C.

*Synthesis of ZnO@C nanocubes.* 240 mg of Zn(NO$_3$)$_2$·6H$_2$O and 4 mg of CTAB were dissolved in 8 mL purified water to obtain a homogeneous solution. The above solution was rapidly poured into 56 mL of aqueous solution with 3.632 g of 2-MeIM under vigorous stirring at room temperature for 0.5 h. The resultant mixture (denoted as Zn-MOF) was centrifuged and the obtained white precipitate was washed with water, and then dried in an oven at 60 °C overnight. Finally, the Zn-MOF was carbonized at 600 °C for 2 h with a heating rate of 5 °C min$^{-1}$ under Ar to obtain ZnO@C.

*Synthesis of carbon nanocubes.* The Zn-MOF was carbonized at 950 °C for 2 h with a heating rate of 5 °C min$^{-1}$ under Ar to obtain carbon NCs. The pyrolysis at 950 ºC is accompanied with evaporation of Zn ions in Zn-MOF precursors (boiling point of Zn: 907 °C), resulting in carbon NCs.

*Synthesis of In$_2$O$_3$ nanoparticles.* 240 mg of In(NO$_3$)$_3$ and 4 mg of CTAB were dissolved in 8 mL purified water to obtain a homogeneous solution. The above solution was rapidly poured into 56 mL of aqueous solution with 3.632 g of 2-MeIM under

vigorous stirring at room temperature for 0.5 h. The resultant mixture (denoted as In(OH)$_3$ NPs) was centrifuged and the obtained white precipitate was washed with water, and then dried in an oven at 60 °C overnight. Finally, the In(OH)$_3$ NPs was heated at 600 °C for 2 h with a heating rate of 5 °C min$^{-1}$ under Ar to obtain In$_2$O$_3$ NPs.

*Preparation of working electrodes.* The working electrodes were prepared by dispersing 4 mg of the electrocatalyst powder together with 60 μL of 5 wt% Nafion in 1 mL of 4:1 v/v water/ethanol under ultrasonication to form a uniform catalyst ink, and then 50 μL of the catalyst ink was dropped onto a glassy carbon electrode (1.0 × 1.0 cm$^2$). The loading of catalysts was 0.2 mg cm$^{-2}$.

*Electrochemical measurements.* Electrochemical CO$_2$ reduction was conducted in a gas-tight H-type cell with Nafion 115 membrane to separate the two compartments. A carbon rod and a KCl-saturated Ag/AgCl electrode were used as the counter and reference electrodes, respectively. The calibration of the reference electrode was checked against an RHE and the measured potentials (*vs.* Ag/AgCl) were converted to RHE using the formula $E$(RHE) = $E$(Ag/AgCl) + 0.197 V + 0.0591 × pH. The electrolyte was 0.5 M potassium bicarbonate (KHCO$_3$) saturated with CO$_2$ (pH = 7.4). Before electrolysis, the electrolyte was purged with CO$_2$ gas (99.998%) for at least 30 min. Each compartment contained 35 mL of electrolyte with a 55 mL headspace. The electrolyte in the cathodic compartment was stirred at a rate of 600 rpm to enhance mass transport of CO$_2$ and products around the surface of the working electrode. The electrochemical measurements were carried out using a CHI660e.

*CO$_2$ reduction product analysis.* For product analyses, the CO$_2$ reduction was

performed for 2 h at various potentials in the electrolyte. Gas products were quantified by a gas chromatography system equipped with a HP-plot molesieve (5A) column and a Pulsed Discharge Detector (PDD). Nitrogen (99.999%) and helium (99.999%) were used as the carrier gases, separately. The Faradaic efficiencies of the gas products were calculated as follows:

$$FE_{CO/H_2}(\%) = \frac{n_{CO/H_2} \times N \times F}{Q} \times 100\%$$

where $n_{CO/H2}$ is the measured amount of CO or $H_2$ in the cathodic compartment and $Q$ (A·s) is the total quantity of electric charge, $N$ (2) is the number of electrons required to form a molecule of CO or H2, $F$ is the Faraday constant (96500 C mol$^{-1}$).

Liquid products were collected at the end of electrocatalysis and analyzed by $^1$H NMR (AVANCE III HD 600MHz). For the $^1$H NMR measurement, 0.5 mL of the catholyte was mixed with 0.1 mL of $D_2O$ and 10 μL of dimethylsulfoxide (DMSO, as the internal standard). The concentration of formate was quantitatively determined from its NMR peak area relative to that of the internal standard using the calibration curve from a series of standard HCOONa solutions. The calibration curve was made by measuring standard solutions of formate. The Faradaic efficiencies of liquid products were calculated as follows:

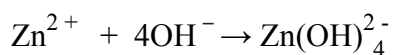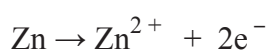$$FE_{HCOO^-}(\%) = \frac{n_{HCOO^-} \times N \times F}{Q} \times 100\%$$

where $n_{HCOO^-}$ is the measured amount of formate in the cathodic compartment and $Q$ (A·s) is the total quantity of electric charge, $N$ (2) is the number of electrons required to form a molecule of formate, $F$ is the Faraday constant (96500 C mol$^{-1}$).

**The cathodic and anodic reactions of the aqueous rechargeable Zn-CO$_2$ battery during charge and discharge processes.** *i) When the aqueous Zn-CO$_2$ battery discharges, the following reactions are assumed to take place:*
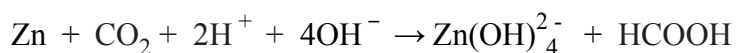
Cathode (CO$_2$-saturated 0.8 M KHCO$_3$, pH = 7.6):

$$CO_2 + 2e^- + 2H^+ \rightarrow HCOOH$$
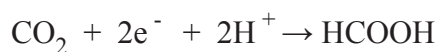
Anode (0.8 M KOH with 0.02 M Zn(CH$_3$COO)$_2$)

$$Zn \rightarrow Zn^{2+} + 2e^-$$

$$Zn^{2+} + 4OH^- \rightarrow Zn(OH)_4^{2-}$$

Overall discharge reaction:

$$Zn + CO_2 + 2H^+ + 4OH^- \rightarrow Zn(OH)_4^{2-} + HCOOH$$

*ii) When aqueous Zn-CO$_2$ battery discharges, the following reactions are assumed to take place:*

Cathode :

$$H_2O \rightarrow \tfrac{1}{2}O_2 + 2H^+ + 2e^-$$

Anode:

$$Zn(OH)_4^{2-} \rightarrow Zn^{2+} + 4OH^-$$

$$Zn^{2+} + 2e^- \rightarrow Zn$$
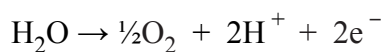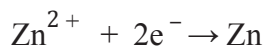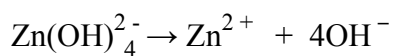
Overall charge reaction:

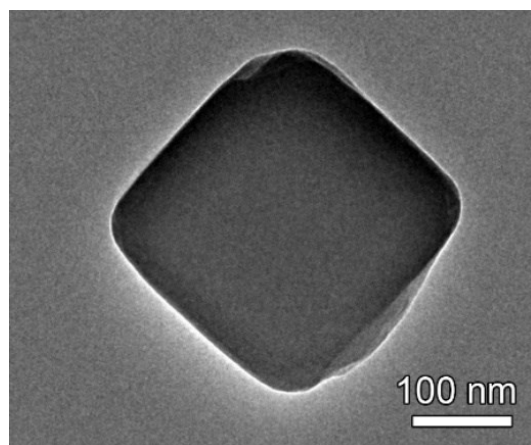$$Zn(OH)_4^{2-} + H_2O \rightarrow Zn + \tfrac{1}{2}O_2 + 2H^+ + 4OH^-$$
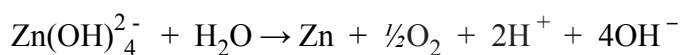
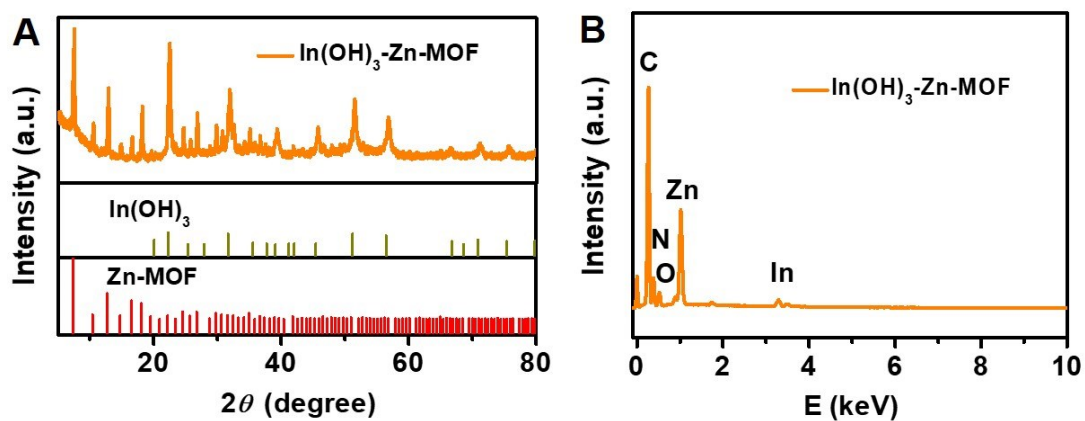**Fig. S1** TEM image of In(OH)$_3$-Zn-MOF.



**Fig. S2** (A) XRD pattern and (B) EDX of In(OH)$_3$-Zn-MOF.
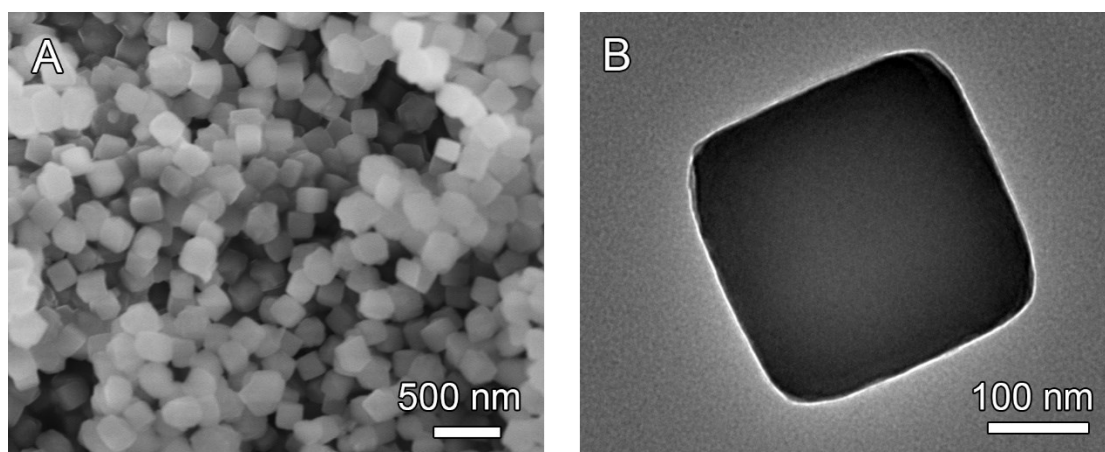


**Fig. S3** (A) SEM and (B) TEM images of Zn-MOF.
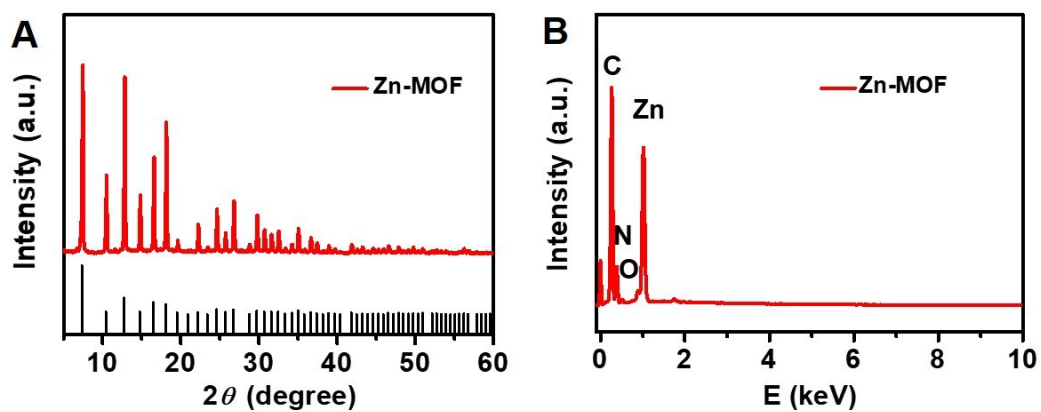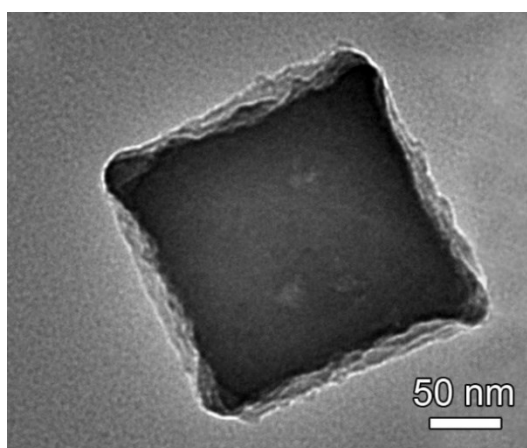
**Fig. S4** (A) XRD pattern and (B) EDX of Zn-MOF.
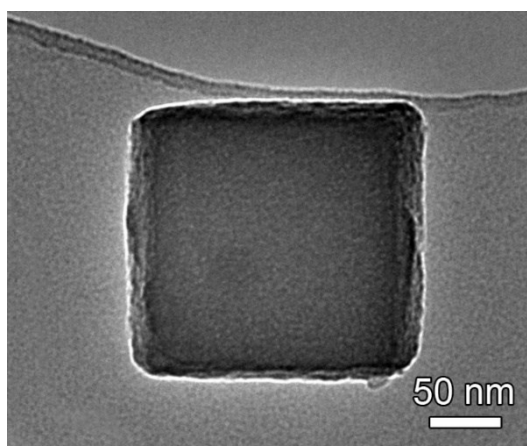


**Fig. S5** TEM image of ZnO@C.



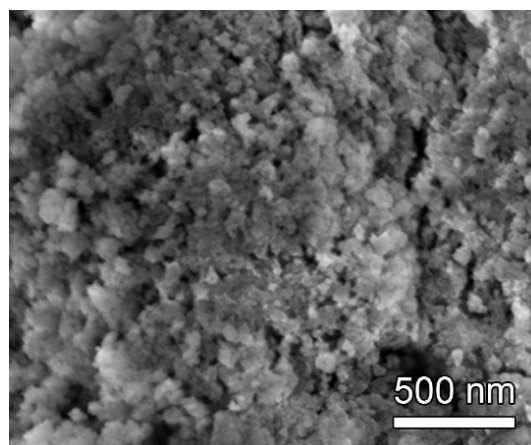**Fig. S6** TEM image of carbon NCs.

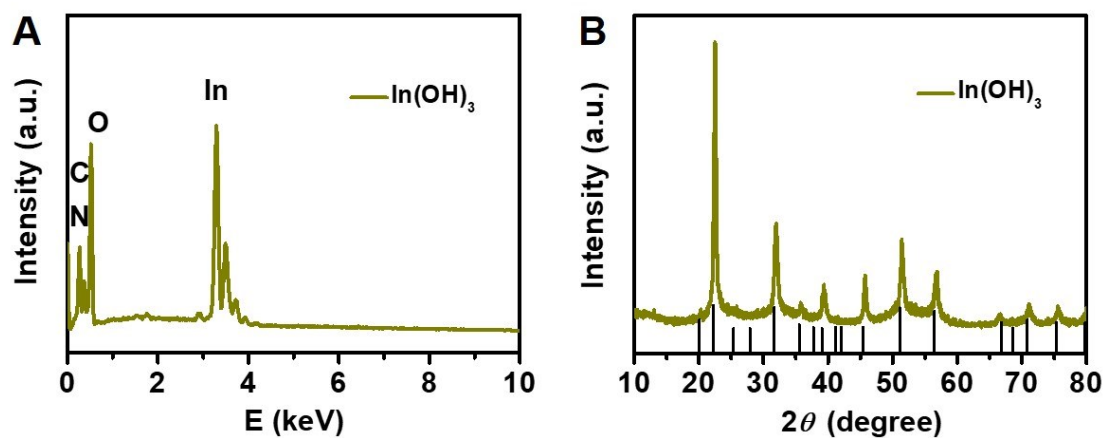**Fig. S7** SEM image of In(OH)$_3$ NPs.



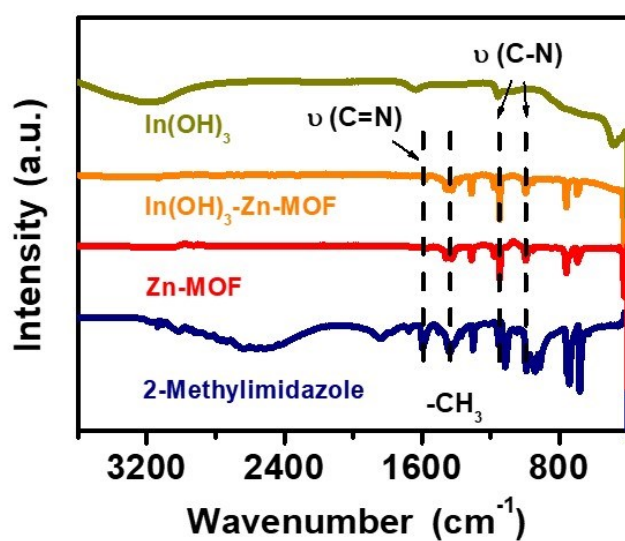**Fig. S8** (A) XRD pattern and (B) EDX of In(OH)$_3$ NPs.



**Fig. S9** FT-IR spectra of 2-Methylimidazole, Zn-MOF, In(OH)$_3$-Zn-MOF and In(OH)$_3$.

The structural variation of precursors was investigated by the Fourier transform infrared (FT-IR) spectra. For 2-Methylimidazole, Zn-MOF, and In(OH)$_3$-Zn-MOF, the peak at 1590 cm$^{-1}$ is due to C=N stretching vibration of imidazole, the peaks at 1143 and 994 cm$^{-1}$ are attributed to C-N stretching vibrations, and the peak at 1436 cm$^{-1}$ is ascribed to the methyl bending vibrational peak. In contrast, these signals are not observed in In(OH)$_3$, indicating the non-coordination between In ions and 2-MeIM.
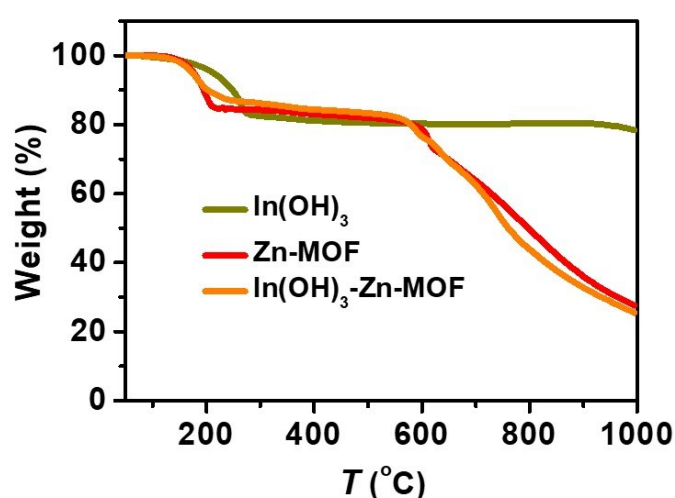


**Fig. S10** TGA curve of In(OH)$_3$-Zn-MOF, Zn-MOF and In(OH)$_3$.

TGA results of In(OH)$_3$-Zn-MOF, Zn-MOF and In(OH)$_3$ are also informative for the combination between In and 2-MeIM. A series of mass-loss occur for In(OH)$_3$-Zn-MOF and Zn-MOF. The initial mass-loss below 300 ℃ is due to the evaporation of pore-occluded solvent, while the subsequent mass-loss regions, at 500-700 ℃ and 700-900 ℃, are attributed to the loss of free rotational methyl groups and framework/ligand decomposition, respectively. The negligible mass-loss for In(OH)$_3$ at the temperature above 300 ℃ is consistent with the non-coordination between In and 2-MeIM.
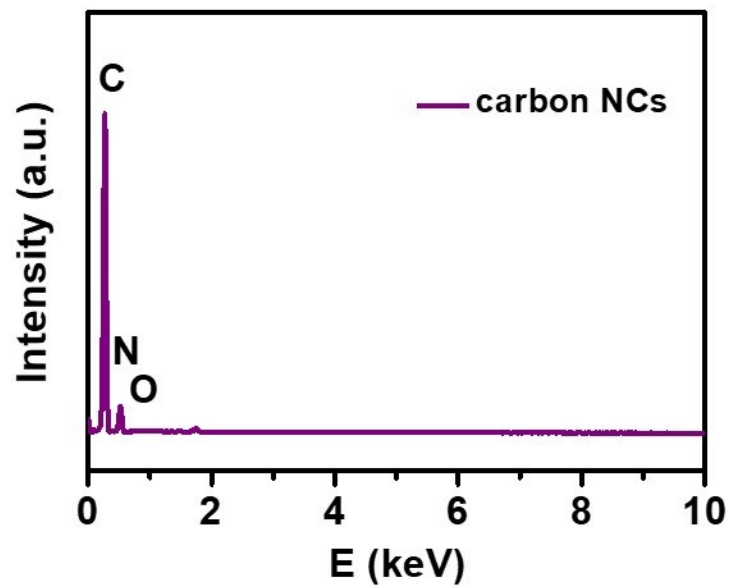
**Fig. S11** EDX of carbon NCs.
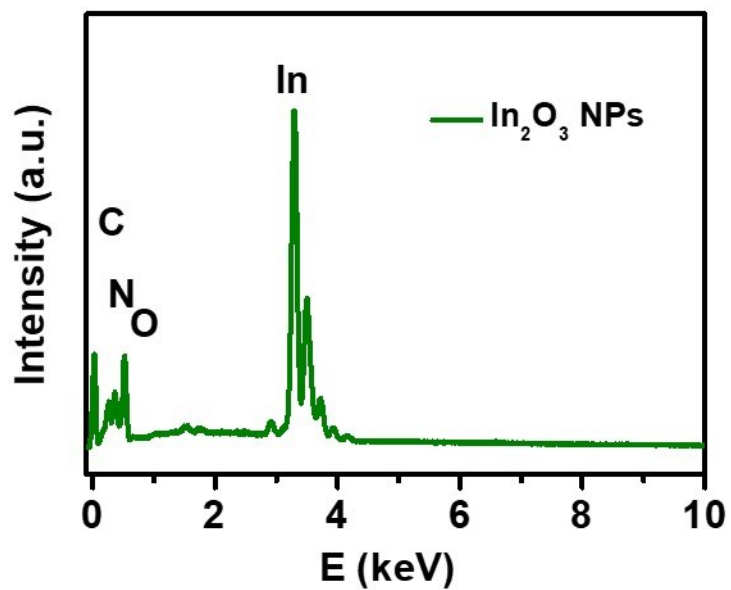


**Fig. S12** EDX of $In_2O_3$ NPs.
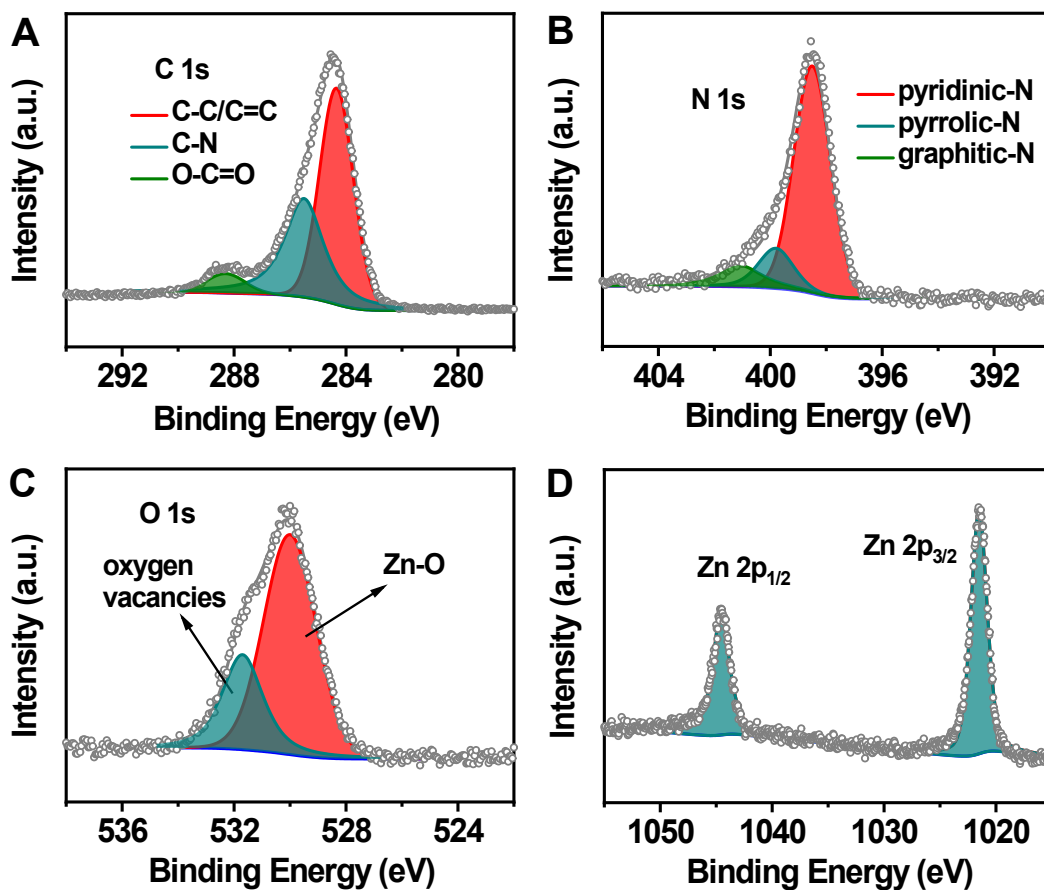
**Fig. S13** High-resolution XPS spectra of (A) C 1s, (B) N 1s, (C) O 1s and (D) Zn 2p for ZnO@C.
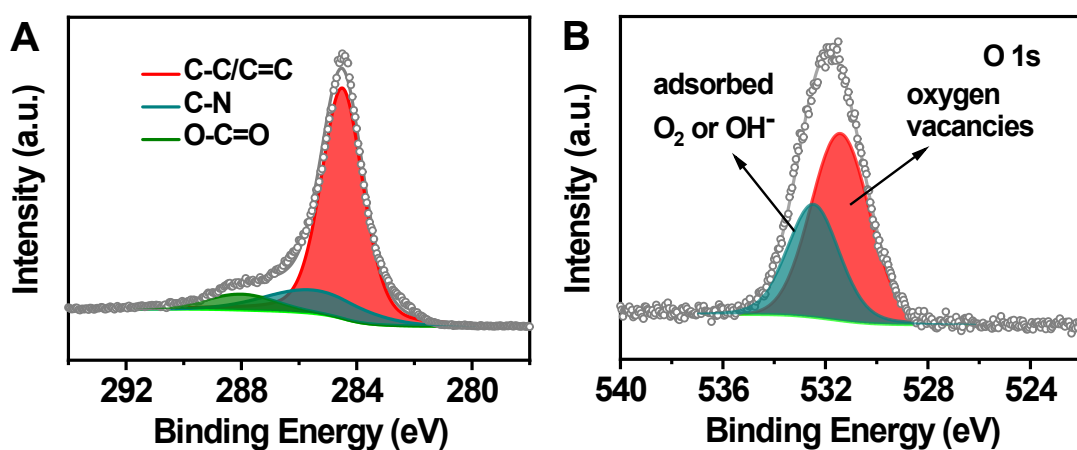


**Fig. S14** High-resolution XPS spectra of (A) C 1s and (B) O 1s for carbon NCs.

The O 1s spectrum of carbon NCs is deconvoluted into adsorbed $O_2$/$OH^-$ and oxygen

vacancies without the bond between metal and oxygen, which verifies the inexistence

of metal.
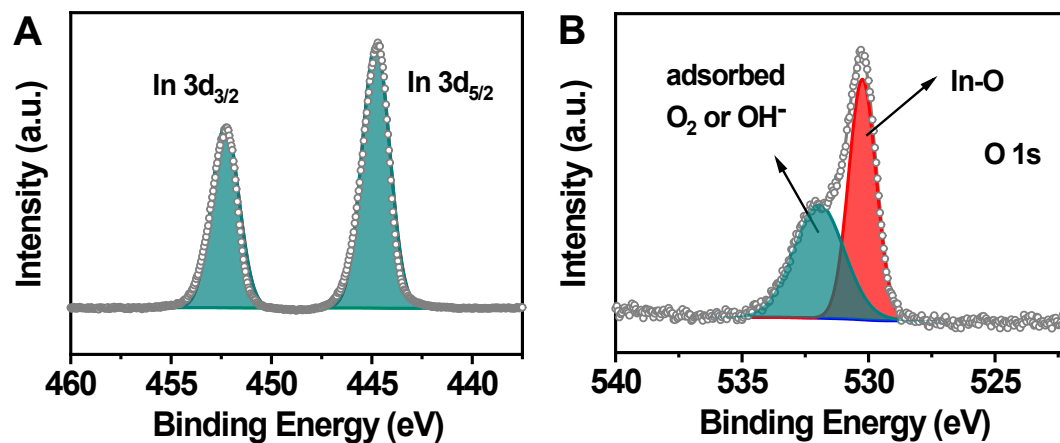


**Fig. S15** High-resolution XPS spectra of (A) In 3d and (B) O 1s for $In_2O_3$ NPs.
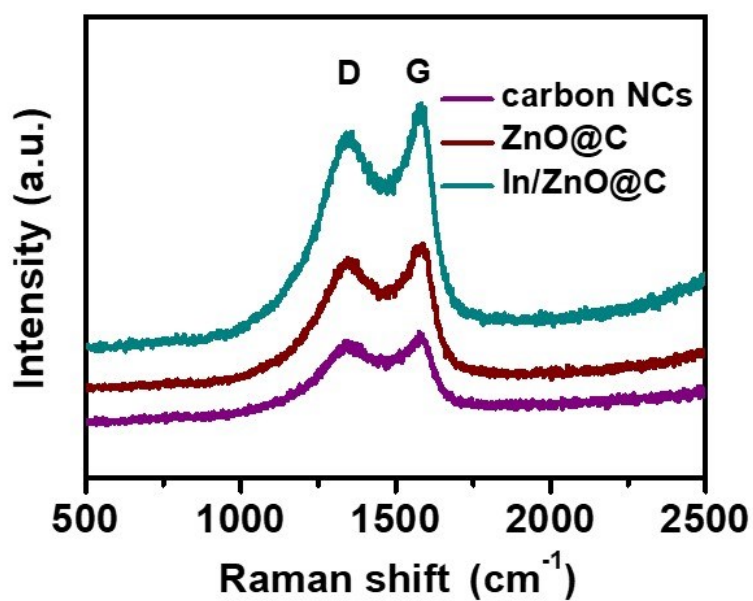


**Fig. S16** Raman spectra of In/ZnO@C, ZnO@C and carbon NCs.
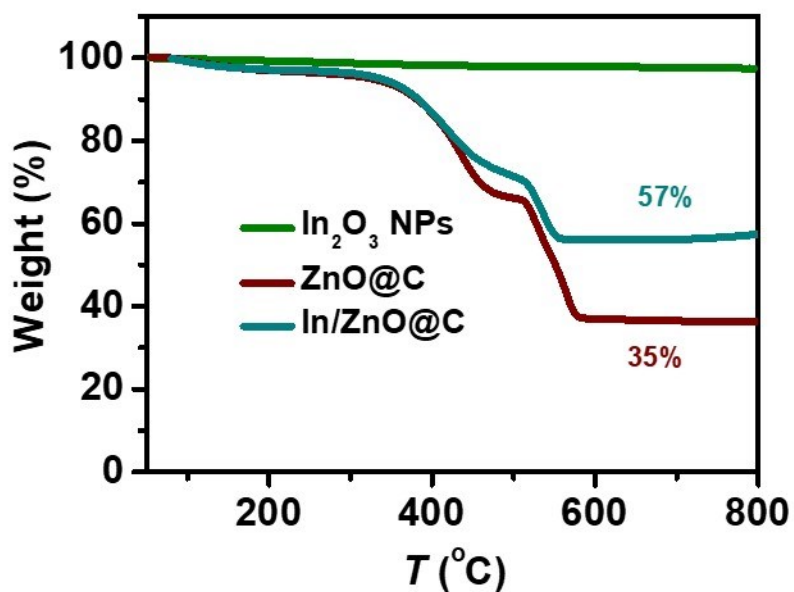
**Fig. S17** TGA curves of In/ZnO@C, ZnO@C and In$_2$O$_3$ NPs in air.
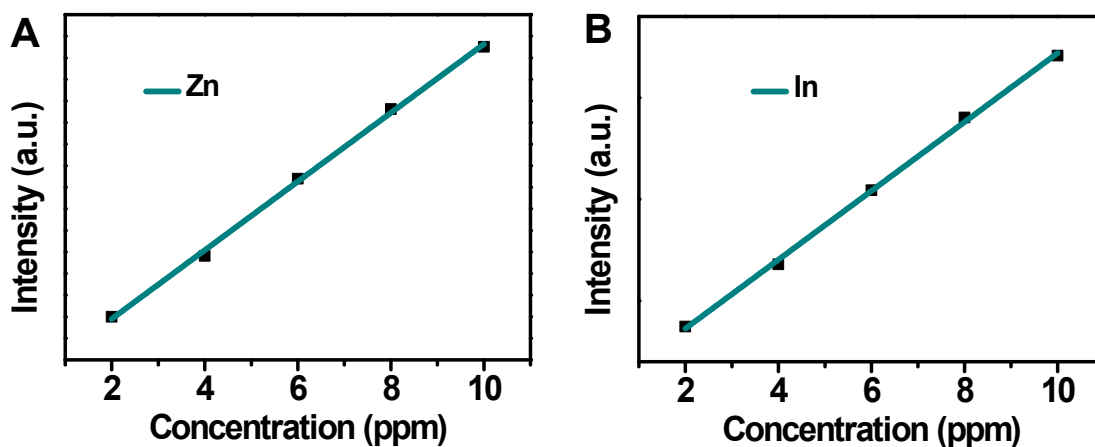


**Fig. S18** The standard curves of (A) In and (B) Zn by ICP-OES.

$$\text{n(In): n(Zn)} = \frac{4.728 \text{ ppm}}{114.818 \text{ g/mol}} : \frac{3.971 \text{ ppm}}{65.38 \text{ g/mol}} = 0.04 : 0.06 = 2:3$$
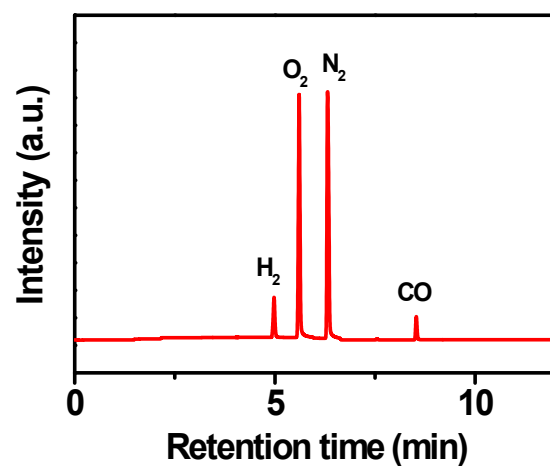
**Fig. S19** Gaseous products of In/ZnO@C in $CO_2$-saturated solution.
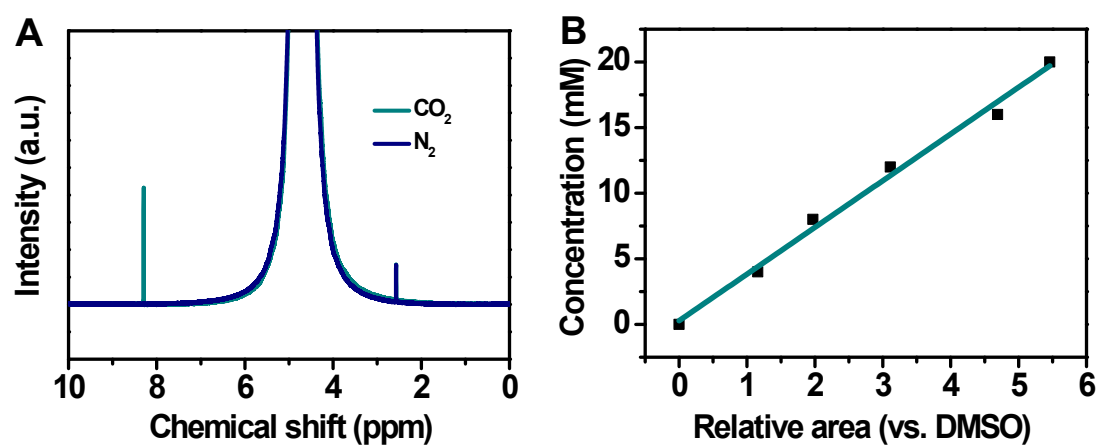


**Fig. S20** (A) Liquid product of In/ZnO@C in $N_2$- and $CO_2$-saturated solution. (B) Standard curve of formate by plotting the formate concentration with respect to the formate/DMSO NMR peak area ratio.
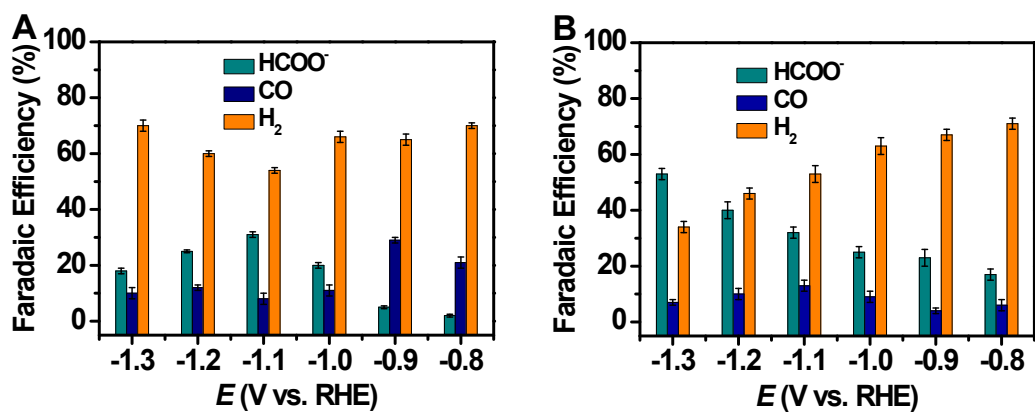
**Fig. S21** Faradaic Efficiencies of HCOO⁻, CO and $H_2$ at different potentials on (A) ZnO@C and (B) $In_2O_3$ NPs.
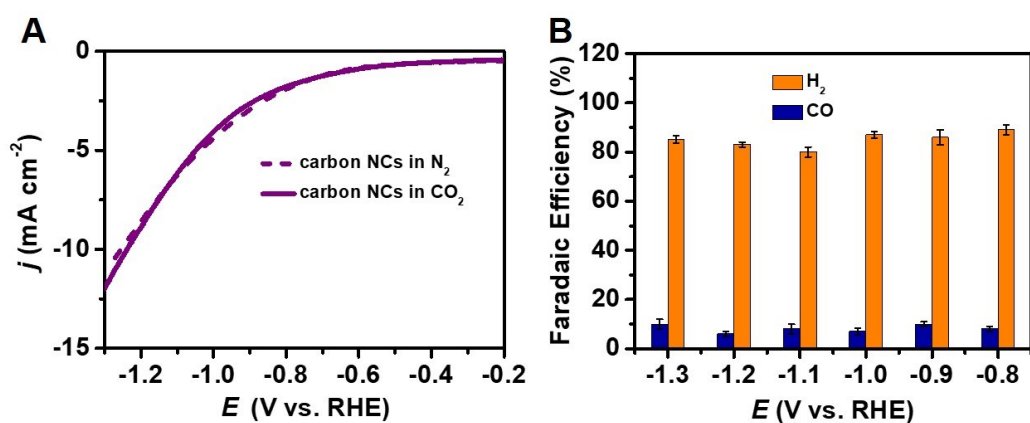


**Fig. S22** (A) LSVs of carbon NCs in $N_2$- and $CO_2$-saturated 0.5 M $KHCO_3$ solutions.

(B) Faradaic efficiency of gaseous products at different potentials on carbon NCs.
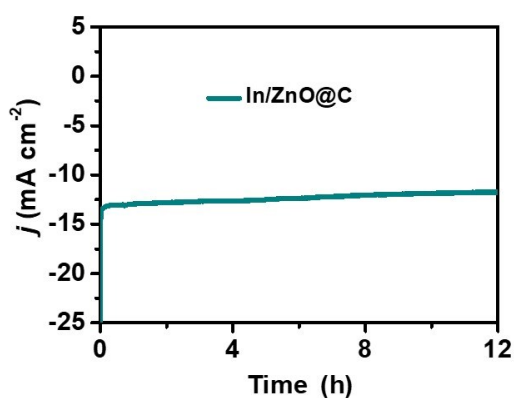


**Fig. S23** Stability measurements over a period of 12 h for electrolysis at -1 V. The

$FE_{HCOO^-}$ is around 70% at -1 V.
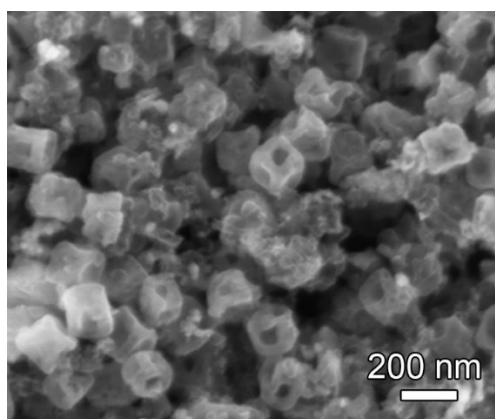
**Fig. S24** SEM image of In/ZnO@C after electrolysis.
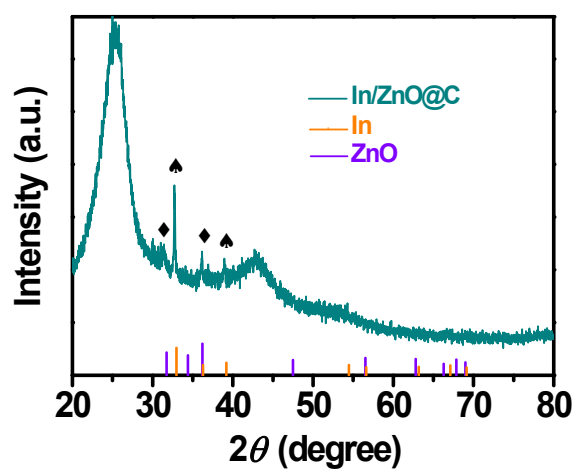


**Fig. S25** XRD pattern of In/ZnO@C after electrolysis. This XRD pattern was obtained with the glassy carbon plate coated with In/ZnO@C. The thin film electrode leads to relatively weak diffraction peaks related to the one in Figure 2A (powder sample).
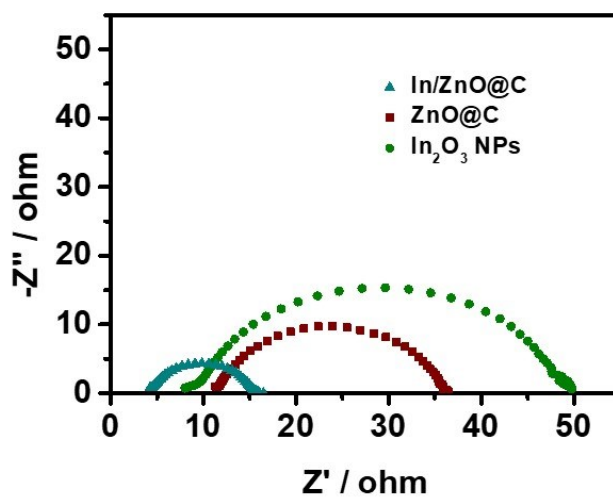
**Fig. S26** EIS curves of different electrodes.
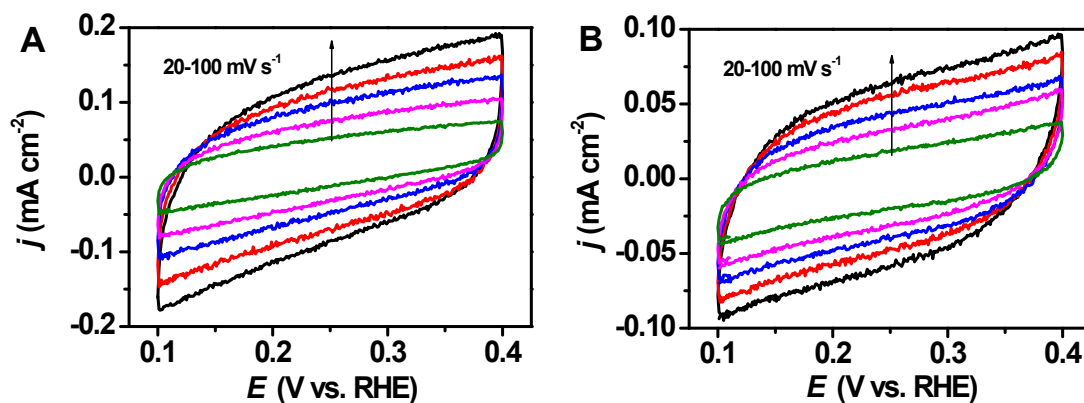


**Fig. S27** CV curves in the range of 0.1 to 0.4 V with different scan rates (20 ~ 100 mV·s$^{-1}$) for (A) In/ZnO@C and (B) In$_2$O$_3$ NPs.
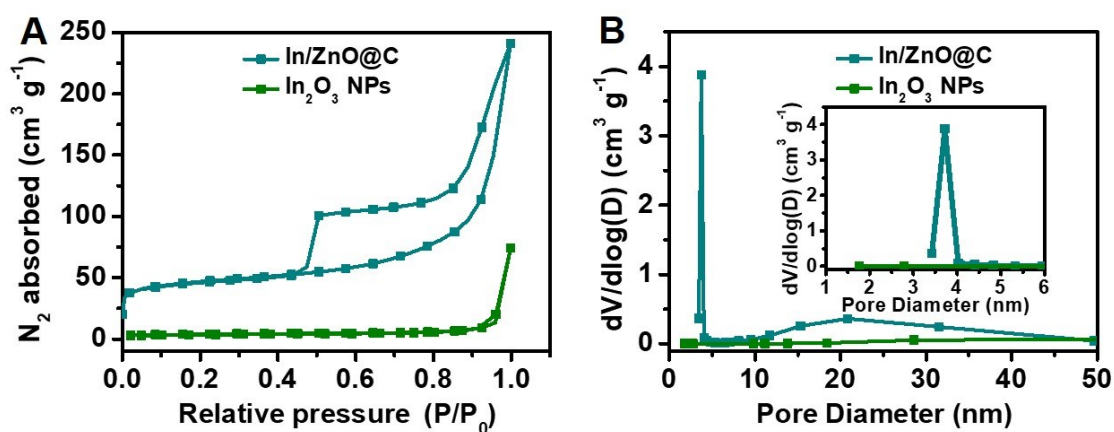


**Fig. S28** (A) N$_2$ adsorption-desorption isotherms and (B) pore size distribution for In/ZnO@C and In$_2$O$_3$ NPs.

**Table S1.** $CO_2RR$ performance of various electrocatalysts.

| Electrocatalysts | Electrolyte | Potential (V vs. RHE) | $FE_{formate}$ | Current Density \|$(mA\ cm^{-2})$\| | Refs. |
|---|---|---|---|---|---|
| Sn/CF | 0.5 M $KHCO_3$ | -1.14 | 80% | 23 | 1 |
| Cu-Sn/rGO | 0.5 M $NaHCO_3$ | -0.99 | 87% | 24 | 2 |
| $ZnSnO_3$ | 0.5 M $NaHCO_3$ | -0.9 | 55% | 3 | 2 |
| $CdSnO_3$ | 0.5 M $NaHCO_3$ | -0.9 | 50% | 6 | 2 |
| Sn modified N-doped carbon nanofiber | 0.5 M $KHCO_3$ | -0.8 | 62% | 9 | 3 |
| $Sn/SnO_x$ thin film | 0.5 M $NaHCO_3$ | -0.7 | 40% | 4 | 4 |
| Electroplated Sn/gas diffusion | 0.5 M $NaHCO_3$ | -1.1 | 71% | 20 | 5 |
| SnO nanoparticles | 0.5 M $KHCO_3$ | -0.86 | 75% | 10 | 6 |
| Sn–Pb alloy on carbon cloth | 0.5 M $KHCO_3$ | -1.37 | 79.8% | 57.3 | 7 |
| Sn/gas diffusion electrode | 0.5 M $KHCO_3$ | -1.17 | 73% | 13.45 | 8 |
| Sn/Nafion gas diffusion electrode | 0.5 M $NaHCO_3$ | -1.17 | 70% | 27 | 9 |
| Sn/gas diffusion electrode | 0.5 M $KHCO_3$ | -1.17 | 78.6% | 22.2 | 10 |
| $Zn_2SnO_4/SnO_2$ | 0.1 M $NaHCO_3$ | -1.08 | 77% | 13 | 11 |
| $Zn_2SnO_4$ | 0.1 M $NaHCO_3$ | -1.08 | 72.65% | 11 | 11 |
| $SnO_2$ | 0.1 M $NaHCO_3$ | -1.08 | 64.91% | 3 | 11 |
| RAD-Zn | 0.5 M $NaHCO_3$ | -1.93 | 87.1% | 14.7 | 12 |

| | | | | | |
|---|---|---|---|---|---|
| D-Zn | 0.5 M NaHCO$_3$ | -1.93 | 67.1% | 4.8 | 12 |
| Pb | 0.1 M KHCO$_3$ | -1.23 | 97.4% | 5 | 13 |
| Hg | 0.1 M KHCO$_3$ | -1.11 | 99.5% | 0.5 | 13 |
| Tl | 0.1 M KHCO$_3$ | -1.2 | 95.1% | 5 | 13 |
| In | 0.1 M KHCO$_3$ | -1.15 | 94.9% | 5 | 13 |
| Sn | 0.1 M KHCO$_3$ | -1.08 | 88.4% | 5 | 13 |
| Cd | 0.1 M KHCO$_3$ | -1.23 | 78.4% | 5 | 13 |
| Bi | 0.1 M KHCO$_3$ | -1.16 | 77% | 1.2 | 13 |
| Bi nanoflake | 0.1 M KHCO$_3$ | -0.6 | 100% | 1 | 14 |
| Bi nanosheets | 0.1 M KHCO$_3$ | -1.1 | 86% | 19 | 15 |
| Ultrathin Bi nanosheets | 0.5 M NaHCO$_3$ | -1 | 100% | 12.5 | 16 |
| In/C | 0.1 M Na$_2$SO$_4$ | -1.2 | 45% | 6.1 | 17 |
| GDE-In$_{0.90}$Sn$_{0.10}$ | 0.1 M KHCO$_3$ | -1.2 | 92% | 16.9 | 18 |
| Zn$_{0.95}$In$_{0.05}$ bimetal | 0.5 M KHCO$_3$ | -1.2 | 95% | 22 | 19 |
| Nanoporous In-Sn | 0.1 M KHCO$_3$ | -1.2 | 78.6% | 12 | 20 |
| In on graphite | 0.05 M KHCO$_3$ | -1.6 | 94.5% | 35 | 21 |
| In$_2$O$_3$-rGO | 0.1 M KHCO$_3$ | -1.2 | 84.6% | 27 | 22 |
| **In/ZnO@C** | **0.5 M KHCO$_3$** | **-1.2** | **90%** | **26** | **This work** |

**Table S2.** Comparison of various Zn-CO$_2$ batteries.

| Cathode | Electrolyte | Open circuit voltage (V) | Peak power density (mW cm$^{-2}$) | Discharge Current Density (mA cm$^{-2}$) | Discharge-Charge Cyclability (h) | Product | Refs. |
|---|---|---|---|---|---|---|---|
| Pd | Catholyte: 1 M NaCl + 0.1 M HCOONa<br>Anolyte: 1 M KOH + 0.02 M CH$_3$CH$_2$ONa | 0.89 | N/A | 0.56 | 33 | HCOOH | 23 |
| Ir@Au | Catholyte: 0.8 M KHCO$_3$<br>Anolyte: 0.8 M KOH + 0.02 M Zn(Ac)$_2$ | 0.76 | N/A | 5 | 30 | CO | 24 |
| NiPG | Catholyte: 3 M KHCO$_3$ + 1.5 M KCl<br>Anolyte: 6 M KOH + 0.2 M Zn(Ac)$_2$ | 0.5 | 0.28 | 0.5 | 13 | CO | 25 |
| SAs-Ni-N-C | Catholyte: 0.5 M KHCO$_3$<br>Anolyte: 5 M KOH + 0.2 M Zn(Ac)$_2$ | 1 | 1.4 | 1 | 32 | CO | 26 |
| Cu–N$_2$/GN | Catholyte: 0.5 M KHCO$_3$<br>Anolyte: 5 M KOH + 0.2 M | 1.77 | 0.62 | 1 | 40 | CO | 27 |

| | | | | | | | |
|---|---|---|---|---|---|---|---|
| | Zn(Ac)$_2$ | | | | | | |
| Fe$_1$NC/S$_1$ | Catholyte: 0.8 M KHCO$_3$ | 0.727 | 0.52 | 0.5 | 25 | CO | 28 |
| | Anolyte: 0.8 M KOH + 0.02 M | | | | | | |
| | Zn(Ac)$_2$ | | | | | | |
| **In/ZnO@C** | **Catholyte: 0.8 M KHCO$_3$** | **1.35** | **1.32** | **1** | **51** | **HCOOH** | **This** |
| | **Anolyte: 0.8 M KOH + 0.02 M** | | | | | | **work** |
| | **Zn(Ac)$_2$** | | | | | | |

**Supplementary References**

1  G. Wen, D. U. Lee, B. Ren, F. M. Hassan, G. Jiang, Z. P. Cano, J. Gostick, E. Croiset, Z. Bai, L. Yang and Z. Chen, Orbital interactions in Bi-Sn bimetallic electrocatalysts for highly selective electrochemical $CO_2$ reduction toward formate production, *Adv. Energy Mater.*, 2018, **8**, 1802427.

2  X. Zhang, F. Li, Y. Zhang, Alan M. Bond and J. Zhang, Stannate derived bimetallic nanoparticles for electrocatalytic $CO_2$ reduction, *J. Mater. Chem. A*, 2018, **6**, 7851-7858.

3  Y. Zhao, J. Liang, C. Wang, J. Ma and G. G. Wallace, Tunable and efficient tin modified nitrogen-doped carbon nanofibers for electrochemical reduction of aqueous carbon dioxide, *Adv. Energy Mater.*, 2018, **8**, 1702524.

4  Y. Chen and M. W. Kanan, Tin oxide dependence of the $CO_2$ reduction efficiency on tin electrodes and enhanced activity for tin/tin oxide thin-film catalysts, *J. Am. Chem. Soc.*, 2012, **134**, 1986-1989.

5  E. Irtem, T. Andreu, A. Parra, M. D. Hernandez-Alonso, S. Garcia-Rodriguez, J. M. Riesco-Garcia, G. Penelas-Perez and J. R. Morante, Low-energy formate production from $CO_2$ electroreduction using electrodeposited tin on GDE, *J. Mater. Chem. A*, 2016, **4**, 13582-13588.

6  J. Gu, F. Héroguel, J. Luterbacher and X. Hu, Densely Packed, Ultra small SnO nanoparticles for enhanced activity and selectivity in electrochemical $CO_2$ reduction, *Angew. Chem., Int. Ed.*, 2018, **130**, 2993-2997.

7  S. Y. Choi, S. K. Jeong, H. J. Kim, I.-H. Baek and K. T. Park, Electrochemical

reduction of carbon dioxide to formate on tin–lead alloys, *ACS Sustain. Chem. Eng.*, 2016, **4**, 1311-1318.

8 Q. Wang, H. Dong and H. Yu, Fabrication of a novel tin gas diffusion electrode for electrochemical reduction of carbon dioxide to formic acid, *RSC Adv.*, 2014, **4**, 59970-59976.

9 G. K. S. Prakash, F. A. Viva and G. A. Olah, Electrochemical reduction of $CO_2$ over Sn-Nafion® coated electrode for a fuel-cell-like device, *J. Power Sources*, 2013, **223**, 68-73.

10 Q. Wang, H. Dong and H. Yu, Development of rolling tin gas diffusion electrode for carbon dioxide electrochemical reduction to produce formate in aqueous electrolyte, *J. Power Sources*, 2014, **271**, 278-284.

11 K. Wang, D. Liu, P. Deng, L. Liu, S. Lu, Z. Sun, Y. Ma, Y. Wang, M. Li, B. Y. Xia, C. Xiao and S. Ding, Band alignment in $Zn_2SnO_4/SnO_2$ heterostructure enabling efficient $CO_2$ electrochemical reduction, *Nano Energy*, 2019, **64**, 103954.

12 T. Zhang, H. Zhong, Y. Qiu, X. Li and H. Zhang, Zn electrode with a layer of nanoparticles for selective electroreduction of $CO_2$ to formate in aqueous solutions, *J. Mater. Chem. A*, 2016, **4**, 16670-16676.

13 Y. Hori, Electrochemical $CO_2$ reduction on metal electrodes, 2008, **42**, 89-189.

14 S. Kim, W. J. Dong, S. Gim, W. Sohn, J. Y. Park, C. J. Yoo, H. W. Jang and J.-L. Lee, Shape-controlled bismuth nanoflakes as highly selective catalysts for electrochemical carbon dioxide reduction to formate, *Nano Energy*, 2017, **39**, 44-52.

15 W. Zhang, Y. Hu, L. Ma, G. Zhu, P. Zhao, X. Xue, R. Chen, S. Yang, J. Ma, J. Liu and Z. Jin, Liquid-phase exfoliated ultrathin Bi nanosheets: uncovering the origins of enhanced electrocatalytic $CO_2$ reduction on two-dimensional metal nanostructure, *Nano Energy*, 2018, **53**, 808-816.

16 N. Han, Y. Wang, H. Yang, J. Deng, J. Wu, Y. Li and Y. Li, Ultrathin bismuth nanosheets from in situ topotactic transformation for selective electrocatalytic $CO_2$ reduction to formate, *Nat. Commun.*, 2018, **9**, 1320.

17 Z. Bitar, A. Fecant, E. Trela-Baudot, S. Chardon-Noblat and D. Pasquier, Electrocatalytic reduction of carbon dioxide on indium coated gas diffusion electrodes-comparison with indium foil, *Appl. Catal. B-Environ.*, 2016, **189**, 172-180.

18 Q. Lai, N. Yang and G. Yuan, Highly efficient In-Sn alloy catalysts for electrochemical reduction of $CO_2$ to formate, *Electrochem. Commun.*, 2017, **83**, 24-27.

19 I. S. Kwon, T. T. Debela, I. H. Kwak, H. W. Seo, K. Park, D. Kim, S. J. Yoo, J.-G. Kim, J. Park and H. S. Kang, Selective electrochemical reduction of carbon dioxide to formic acid using indium-zinc bimetallic nanocrystals, *J. Mater. Chem. A*, 2019, **7**, 22879-22883.

20 W. J. Dong, C. J. Yoo and J. L. Lee, Monolithic nanoporous In-Sn alloy for electrochemical reduction of carbon dioxide, *ACS Appl. Mater. Interfaces*, 2017, **9**, 43575-43582.

21 R. Hegner, L. F. M. Rosa and F. Harnisch, Electrochemical $CO_2$ reduction to

formate at indium electrodes with high efficiency and selectivity in pH neutral electrolytes, *Appl. Catal. B-Environ.*, 2018, **238**, 546-556.

22 Z. Zhang, F. Ahmad, W. Zhao, W. Yan, W. Zhang, H. Huang, C. Ma and J. Zeng, Enhanced electrocatalytic reduction of $CO_2$ via chemical coupling between indium oxide and reduced graphene oxide, *Nano Lett.*, 2019, **19**, 4029-4034.

23 J. Xie, X. Wang, J. Lv, Y. Huang, M. Wu, Y. Wang and J. Yao, Reversible aqueous zinc-$CO_2$ batteries based on $CO_2$-HCOOH interconversion, *Angew. Chem., Int. Ed.*, 2018, **57**, 16996-17001.

24 X. Wang, J. Xie, M. A. Ghausi, J. Lv, Y. Huang, M. Wu, Y. Wang and J. Yao, Rechargeable Zn-$CO_2$ electrochemical cells mimicking two-step photosynthesis, *Adv. Mater.*, 2019, **31**, 1807807.

25 R. Yang, J. Xie, Q. Liu, Y. Huang, J. Lv, M. A. Ghausi, X. Wang, Z. Peng, M. Wu and Y. Wang, A trifunctional Ni-N/P-O-codoped graphene electrocatalyst enables dual-model rechargeable Zn-$CO_2$/Zn-$O_2$ batteries, *J. Mater. Chem. A*, 2019, **7**, 2575-2580.

26 W. Zheng, F. Chen, Q. Zeng, Z. Li, B. Yang, L. Lei, Q. Zhang, F. He, X. Wu and Y. Hou, A universal principle to accurately synthesize atomically dispersed metal-$N_4$ sites for $CO_2$ electroreduction, *Nano-Micro Lett.*, 2020, **12**, 108.

27 W. Zheng, J. Yang, H. Chen, Y. Hou, Q. Wang, M. Gu, F. He, Y. Xia, Z. Xia, Z. Li, B. Yang, L. Lei, C. Yuan, Q. He, M. Qiu and X. Feng, Atomically defined undercoordinated active sites for highly efficient $CO_2$ electroreduction, *Adv. Funct. Mater.*, 2019, **30**, 1907658.

28 T. Wang, X. Sang, W. Zheng, B. Yang, S. Yao, C. Lei, Z. Li, Q. He, J. Lu, L. Lei, L. Dai and Y. Hou, Gas diffusion strategy for inserting atomic iron sites into graphitized carbon supports for unusually high-efficient $CO_2$ electroreduction and high-performance Zn-$CO_2$ batteries, *Adv. Mater.*, 2020, **32**, 2002430.